

Non-volatile rewritable frequency tuning of a nanoelectromechanical resonator using photoinduced doping

David J. Miller^{1,2,3}, Andrew Blaikie^{1,2,3}, and Benjamín J. Alemán^{1,2,3,4,}*

¹Department of Physics, University of Oregon, Eugene, Oregon, 97403, United States

²Materials Science Institute, University of Oregon, Eugene, Oregon, 97403, United States

³Center for Optical, Molecular, and Quantum Science, University of Oregon, Eugene, Oregon, 97403, United States

⁴Phil and Penny Knight Campus for Accelerating Scientific Impact, University of Oregon, Eugene, Oregon, 97403, United States

KEYWORDS:

Graphene, NEMS, Frequency Tuning, Photodoping

ABSTRACT:

Arrays of nanoelectromechanical resonators (NEMS) have shown promise for a suite of applications, ranging from nanomechanical information processing technologies to high-resolution mass spectroscopy systems. In these arrays, the mechanical resonance frequency can form the base unit of information, like the voltage level in analog electronics. A fundamental challenge towards broader adoption of NEMS arrays is a lack of viable frequency tuning methods, which must simultaneously allow for persistent and reversible control of single resonators while also being scalable to large arrays of devices. In this work, we demonstrate an electro-optic tuning method for graphene-based NEMS that meets these needs. Our method uses a focused laser to locally photoionize defects on an individual resonator. After the laser is turned off, the trapped charge created by photoionization persists and applies spatially localized electrostatic strain to

the resonator, thereby tuning its frequency. Our approach has a persistence time of several days and can repeatedly write and erase the state of a single device with a high degree of precision. We show the scalability of this technique by aligning the frequencies of spatially separated NEMS devices and discuss potential implications of this tuning method when applied to both single devices and to programmable NEMS networks.

MAIN TEXT:

Nanoelectromechanical (NEMS) resonators are among the most sensitive detectors of mass¹, charge², and force³, and have enabled discoveries of nonlinear phenomena⁴ as well as tests of macroscopic quantum mechanics⁵. Much like their electronic device counterparts, the potential of NEMS grows when they are built up into large-scale arrays and networks. These arrays have already enabled neutral mass spectroscopy⁶, and have been proposed for ultralow-power alternatives to traditional analog electronics⁷ as well as nanomechanical information technologies like memory^{8,9}, logic¹⁰, and computing^{11,12}. Moreover, programmable arrays, where the frequency and coupling of each individual resonator are precisely controlled, are expected to enable tunable acoustic bandgaps¹³ and lensing¹⁴, and more exotic systems like topological materials¹⁵, metamaterials¹⁶, and as a potential platform for neuromorphic computing^{17,18} or simulating complex networks¹⁹.

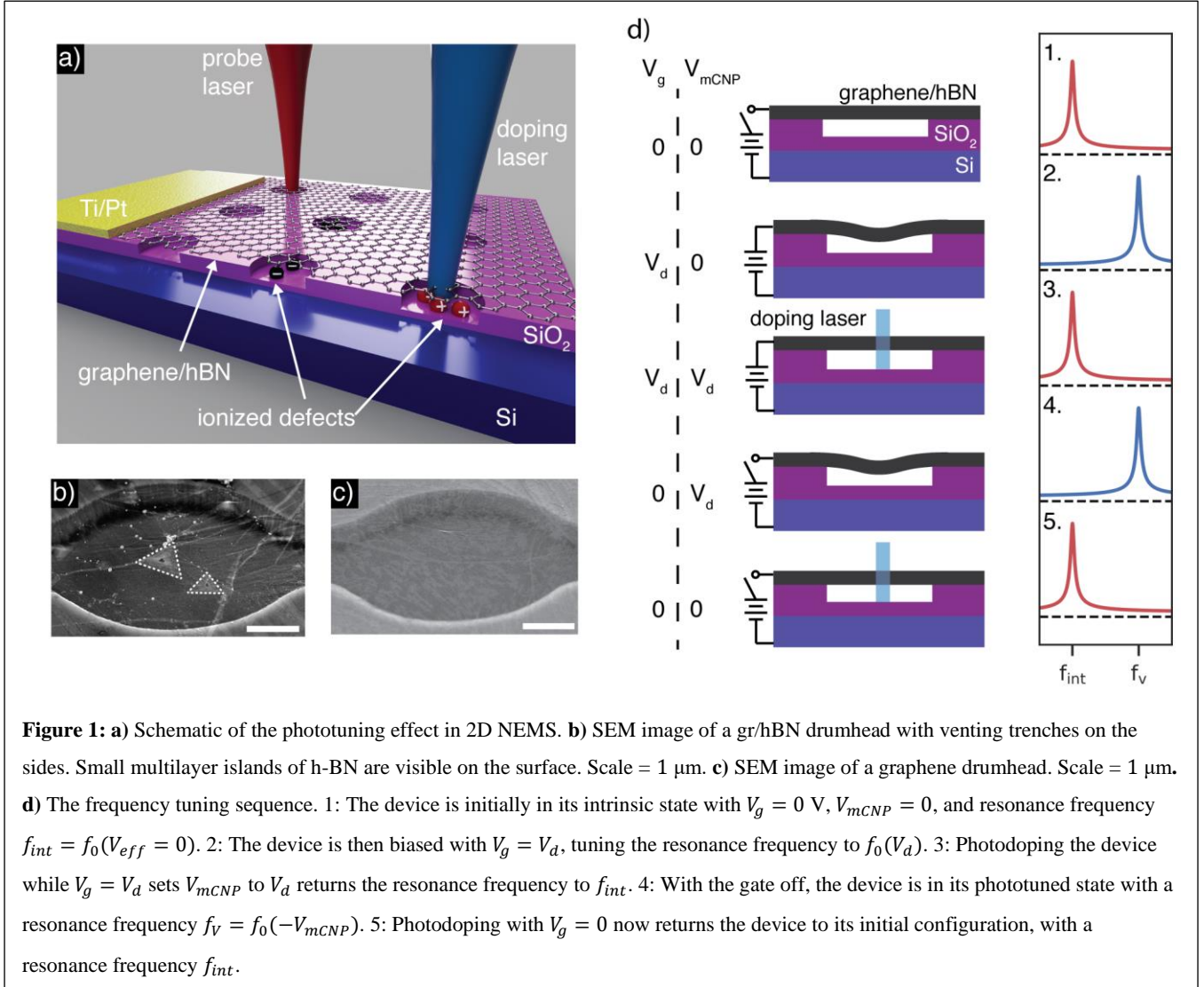
To realize the promise of NEMS arrays, methods are needed to efficiently program and interface with large networks of NEMS. Tuning the resonance frequency of individual NEMS offers one such method but the frequency tuning must be simultaneously persistent (*i.e.* have memory), reversible, fast, and operate over a large frequency range. There have been numerous demonstrations of NEMS tuning methods²⁰, but each is accompanied by significant drawbacks and challenges when applied to large arrays of devices. Active tuning methods, such as electrostatic gating²¹ or local heating²², are reversible and can achieve a large tuning range, but are inherently transient. Thus, to maintain the tuned frequency, active tuning requires a continuous, separate external force for each NEMS resonator, making them impractical for integration into large arrays. In contrast, passive methods permanently modify the NEMS structure, for instance by adding

or removing mass^{23–25}, can achieve persistent tuning but at the expense of rewritability. Several NEMS tuning approaches have attempted to combine persistence and reversibility, including mass electromigration along suspended carbon nanotubes²⁶ and etching/depositing of mass with a focused ion beam²⁷, but these techniques require an electron microscope and *in-situ* nanomanipulation, which severely impedes practicality and scalability. Moreover, these tuning schemes suffer from poor frequency resolution, a limited tuning range ($\sim 10\%$), slow speed, and limited cyclability.

Here, we demonstrate a non-volatile and rewritable frequency tuning method for graphene-based two-dimensional (2D) NEMS^{21,24,28–31}. In our approach, we use a focused laser and two global electrical contacts to create locally photoionized defects^{32–36} on an individual resonator. After the optical and electrostatic fields are removed, the trapped charge created by the photoionization persists and applies spatially localized electrostatic strain to the resonator, thereby tensioning the resonator and tuning its frequency. Our approach is robustly rewritable over a large tuning range and persistent over many days with no need for external power, and is also exceptionally fast and fully scalable to NEMS arrays of arbitrary size. By providing a facile means to locally address the frequency of a NEMS resonator, this work lays the groundwork for fully programmable large-scale NEMS lattices and networks^{16,37}.

Our frequency tuning method relies on principles similar to electrostatic gate-tuning^{21,24}, which is among the most commonly used active tuning methods. In a typical gate-tuning configuration, a NEMS device is suspended above a gate electrode to form a simple parallel-plate capacitor. An electrostatic potential will tension the membrane and tune the resonance frequency to a value $f_0(V_g) \propto \frac{1}{2} \frac{dC_g}{dx} (V_g - V_{mCNP})^2$, where V_g is the external gate voltage and V_{mCNP} is called the mechanical charge neutrality point, which is analogous to the electronic charge neutrality point³⁸. Non-zero values of V_{mCNP} , have routinely been observed in 2D NEMS^{24,30} and are typically ascribed to the presence of charged defects. In this case, the effective voltage experienced by the membrane is $V_{eff} = V_g - V_{mCNP}$. Although tuning f_0 with an external V_g is

commonplace, tuning f_0 by controllably modifying V_{mCNP} has not previously been explored and forms the basis of this work.



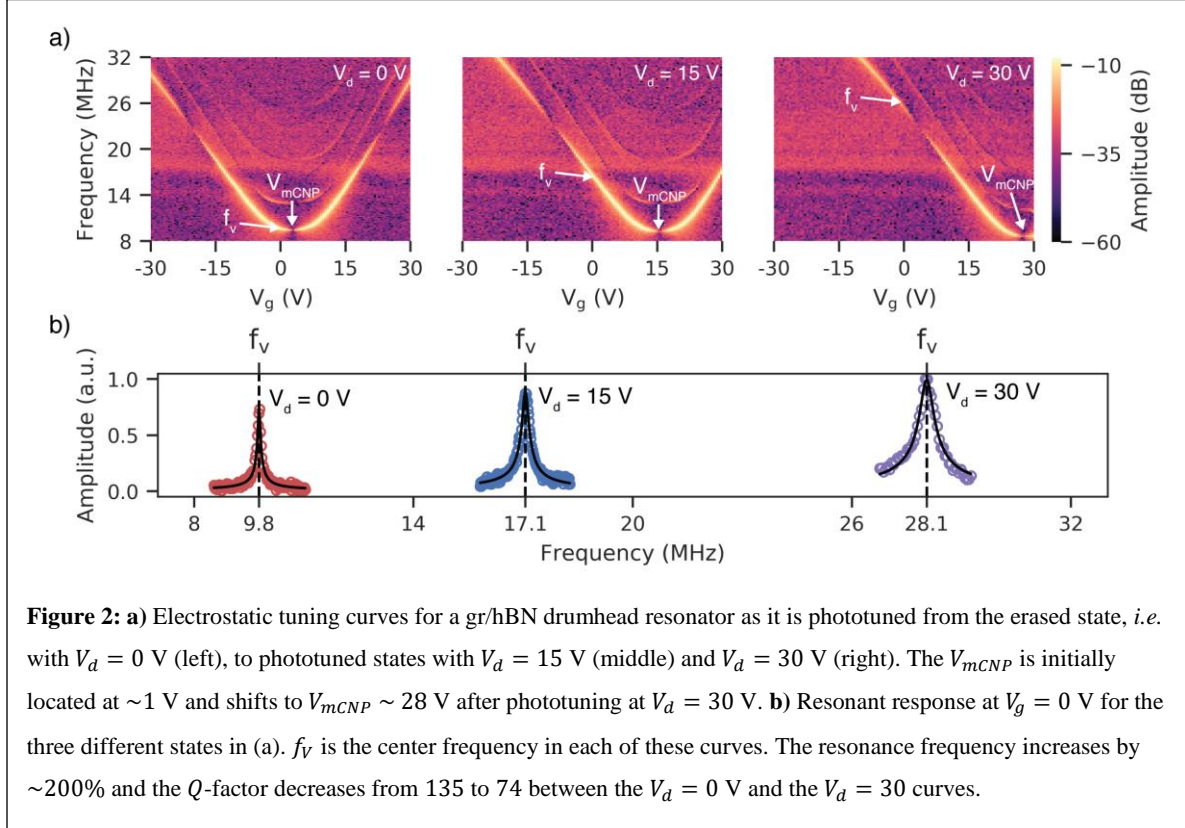
We tune V_{mCNP} of an individual 2D NEMS device with spatially resolved photodoping^{32–36}. In previous studies of photodoping in graphene, graphene is separated from a global gate-electrode by a stack of dielectrics with varying bandgaps³⁴. Simultaneous application of a gate-voltage and a focused laser causes ionized defects to accumulate at the laser focus, shifting the electronic charge neutrality point until the applied gate voltage is neutralized. Crucially, the charge remains trapped after the laser and gate are removed, allowing for intricate, doping patterns to be patterned into the heterostructure. By applying the

same principle to suspended graphene NEMS, we can controllably modify V_{mCNP} using only a focused laser and a single global gate voltage V_g , allowing us to tune f_0 in an arbitrarily large array of devices.

We study this tuning method in NEMS membranes made from both CVD-grown monolayer graphene and a graphene/hBN heterostructure (gr/hBN). Our devices consist of the two-dimensional sheet suspended over $\sim 4 - 5 \mu\text{m}$ diameter circular cavities etched into SiO_2 on top of a degenerately doped silicon gate electrode (see Figure 1a-c). A layer of SiO_2 ($\sim 300 \text{ nm}$ thick) is left at the bottom of the cavities to prevent shorting and create potential charge traps³³. The devices are driven with standard electrostatic actuation techniques²¹ using the silicon back-gate and a Ti/Pt top contact, and measured using an interferometer operating at 633 nm ^{28,31}. Photodoping is typically performed with a power-stabilized 445 nm diode laser except where noted otherwise.

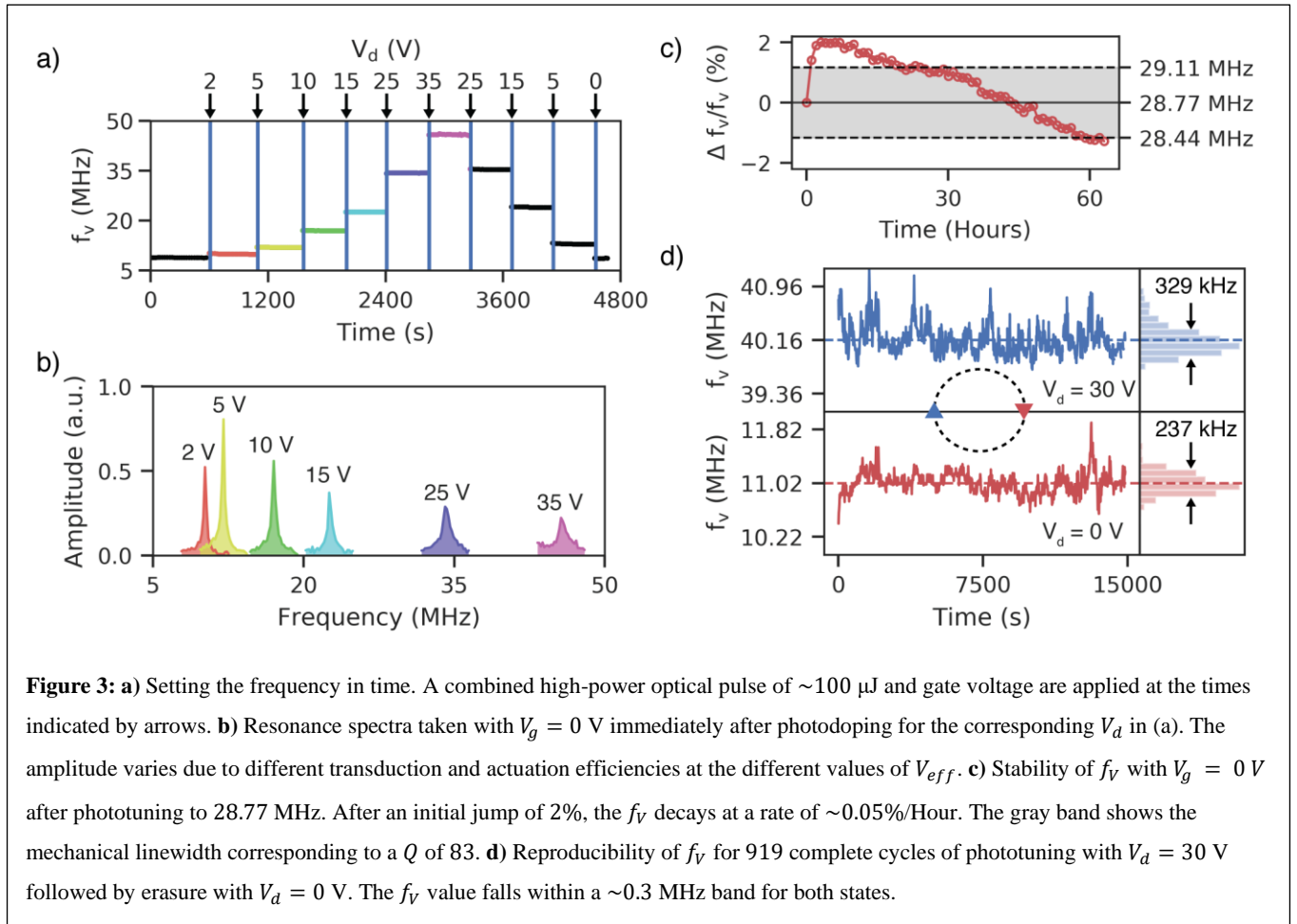
To set or change the frequency of an individual membrane through photodoping—a process we call phototuning—we apply a bias to a global back-gate (in this case, degenerately doped silicon) while focusing a laser onto the individual, suspended membrane of interest (see Figure 1d). Prior to any photodoping and assuming an initial V_{mCNP} of 0 V , the resonator will be at its intrinsic resonance frequency $f_{int} = f_0(0)$ before the laser or bias are turned on (*step 1*). Then, we set the gate voltage to a value V_d , tensioning the membrane and blue shifting the resonance frequency (*step 2*) from f_{int} to $f_0(V_d)$. Next, with the bias still at V_d , we turn the laser on to start the charge-trapping process. This brings V_{mCNP} towards V_d , lowering V_{eff} , and red shifting the resonance frequency. Given enough laser dose, V_{mCNP} saturates at V_d and the frequency returns to f_{int} (*step 3*). After turning the laser and bias off, the frequency immediately blue shifts to $f_0(-V_d)$ (*step 4*), which is the same as $f_0(V_d)$ due to the symmetry of $f_0(V_{eff})$. The phototuned frequency obtained after *step 4* does not require an external gate bias to maintain and is denoted $f_V = f_0(-V_{mCNP})$. Steps 1-4 complete the phototuning “write” function. The frequency can be reset back to f_{int} —or “erased”—by zeroing the bias voltage ($V_d = 0 \text{ V}$) and illuminating the membrane with the laser (*step 5*). We note that the description above represents the ideal case of phototuning. For most devices we

study, V_{mCNP} is initially slightly offset from zero and V_{mCNP} saturates at a slightly different value than V_d , but neither of these factors affect the crucial properties of the phototuning method.



The fundamental effects of phototuning are revealed in the gate voltage tuning curves and frequency response spectra. We show gate curves for a gr/hBN device in the erased state ($V_d = 0$ V) and two tuned states ($V_d = 15, 30$ V), in Figure 2a. For these measurements, the membrane was photodoped to saturation by rastering the laser over the area of the drumhead at relatively high power (~ 1 mW/ μm^2). The fundamental mode is the easiest to resolve, but several higher order modes are also present. The curve shapes are consistent with an electrostatically biased membrane^{21,24}. In the erased state, V_{mCNP} is offset from zero by ~ 1 V, which is common and indicates the presence of static charged contaminants. With $V_d = 30$ V, V_{mCNP} saturates to ~ 28 V, where the new potential arises from charged defects in the h-BN^{32,34} and the oxide³³. Although V_{mCNP} differs by ~ 27 V between these states, the gate-dependence of each mode relative to V_{mCNP} doesn't change. Thus, apart from the V_{mCNP} shift, the phototuning process does not alter the mechanical characteristics of the device in a significant way, unlike most passive tuning methods^{22,25}.

The individual resonance curves corresponding to the three states are shown in Figure 2b. As V_{mCNP} is tuned from ~ 1 V to ~ 28 V, f_V increases from ~ 9.8 MHz to ~ 28.1 MHz, a change of $\sim 200\%$. The Q of the 28.1 MHz peak ($Q = 74$) is smaller than that of the 9.8 MHz peak ($Q = 135$), just as in the case of an applied electrostatic backgate²⁹. Although the central focus of this work is to report the phototuning effect, it also reveals that measuring or driving²¹ 2D NEMS with an optical probe can lead to unintended frequency drift.



To demonstrate the reversibility of f_V using phototuning, we change f_V at discrete time intervals by varying the doping potential. At the beginning of each interval, we phototune the device using a single short, high power laser pulse (~ 2 mW, 0.5 s) at a given V_d (Figure 3a), and then continuously monitor the f_V by fitting the resonance spectra (Figure 3b) for the remainder of the interval, ~ 600 seconds. Increasing V_d stepwise

from 0 to 35 V (as seen in Figure 3a), f_V takes on fixed, stable values that increase from 7 MHz up to 45 MHz. When we decrease V_d stepwise back to 0 V, f_V returns to 7 MHz. This data clearly demonstrates that the phototuning of f_V is both reversible and bidirectional. The tuning range of f_V is large, here nearly 550%, which is an order of magnitude larger than previous hybrid tuning methods^{26,27}. For a quality factor of a typical device ($Q \sim 100$), this tuning range equals 543 resonance linewidths. In our measurements we limited the doping potential to 35 V to avoid damage to the mechanical resonators, but larger potentials up to the dielectric breakdown of the SiO₂ could be used to achieve an even higher degree of tuning.

The frequency phototuning method is persistent. This persistence is clear from the steps in Figure 3a, which show f_V is stable for at least 600 s. To assess the longer-term stability of phototuning, we write f_V a single time and then measure f_V every hour over the course of 3 days. Figure 3c plots the fractional change $\Delta f_V / f_V$ after phototuning f_V with a doping potential of 30 V. Initially, f_V blueshifts by 2% over the course of 2 hours. After this initial detuning, the device slowly relaxes and f_V redshifts at a rate of 0.05%/hour. For reference, the mechanical linewidth for our devices is $\sim 2\%$ of the resonance frequency (shaded region of Figure 3b), so the frequency shifts by a linewidth in ~ 40 hours. This long-lived state does not require an external power supply or gate bias. Therefore, phototuning can replace patterned gate electrodes^{13,37}, even in arbitrarily large resonator arrays. To isolate the effect of the probe laser, which will cause some detuning, we set f_V and measure it once after 8 days (See supporting information). We still observe a small amount of detuning in addition to warping of the gate tuning spectrum. Therefore, additional sources of detuning are present and may include the rearrangement of the trapped charge in the oxide or h-BN, or strain relaxation (*e.g.* in folds and edge clamping). Improved stability would likely be possible at cryogenic temperatures, which would reduce thermally-induced recombination of the ionized defects³². Given the time scale of the drift, phototuning feedback would be a straightforward means to stabilize the frequency.

The phototuning method can achieve a high degree of frequency tuning repeatability and can execute an indefinite number of write/erase cycles with no observable change to the mechanical properties of the NEMS device. To test repeatability and cycling performance, we erase the frequency state by phototuning

with $V_d = 0$ V, then we write f_V with $V_d = 30$ V. For all writing and erasure steps, the same dose of ~ 2 mW over 0.5 s was used. Figure 3c shows the results after 919 erase/write cycles. As measured from the histogram (right of Figure 3d), the average frequencies of erased and written states are $f_{erase} = 11.02 \pm 0.12$ MHz and $f_{write} = 40.16 \pm 0.16$ MHz, which yields a writing repeatability of 99.5%. The small uncertainty in the repeatability could be inherent to the phototuning process, but could also be caused by sources of frequency noise and fluctuations common to 2D NEMS, such as adsorbates, heating, and unwrinkling³¹, or fluctuations in the power of doping laser. The large frequency separation of the written and erased states in Figure 3a and Figure 3c could easily allow a discrete binary logic state^{8,39} or, given the measured error of 160 KHz, over 150 discrete and well-defined logic states.

The temporal rate of the phototuning method is exceptionally fast. The phototuning rate can be inferred from the time-dependence of either f_V or V_{mCNP} during the phototuning process (see supporting information). Figure 4a shows a plot of $V_{mCNP}(t)$ (blue, upper) and $f_V(t)$ (orange, lower) for $V_d = 9$ V, and $P \sim 530$ μ W with a 445 nm laser. Both V_{mCNP} and f_V approach steady state saturation values within ~ 10 ms. As noted earlier, we find that V_{mCNP} does not saturate exactly to V_d , but each device has a small but consistent offset, which we denote δV_{mCNP} . To obtain the doping rate, we approximate $V_{mCNP}(t)$ with a saturation function of the form,

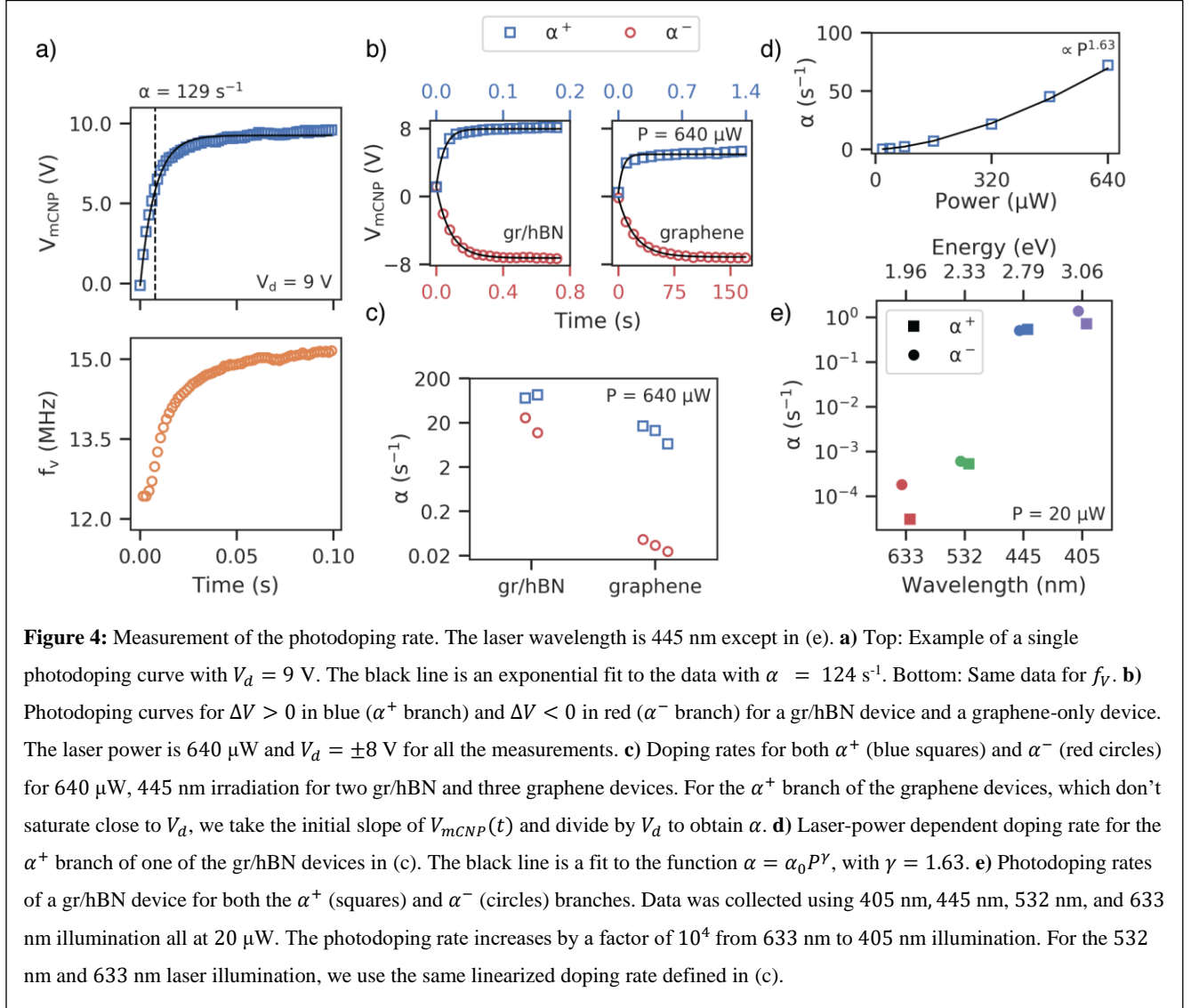
$$V_{mCNP}(t) = \Delta V(1 - e^{-\alpha t}) + V_0 \quad (1)$$

where $\Delta V \approx V_d - V_0 + \delta V_{mCNP}$, V_0 is fixed at the initial V_{mCNP} , and α is the doping rate, which depends on the laser's power, wavelength, and position^{35,36}. Prior to each rate measurement, the device is photodoped at high power with $V_d = 0$ V, which initializes V_0 to δV_{mCNP} . The black trace in the upper plot of Figure 3a is the fit for $V_{mCNP}(t)$ using Eq. 1, with fit parameters $\Delta V = 8.94$ V and $\alpha = 129$ s⁻¹. In this model, the instantaneous doping rate is $\left| \frac{dV_{mCNP}(0)}{dt} \right| = |\Delta V|\alpha$, and the frequency tuning rate is $R_f \equiv \left| \frac{dV_{mCNP}(0)}{dt} \right| \frac{df_0}{dV_g} = \alpha |\Delta V| \frac{df_0}{dV_g}$, where $\frac{df_0}{dV_g}$ is the slope of the photodoped gate voltage tuning curve at $V_g = 0$ V (*i.e.* at f_V). With

$|V_{mCNP}| \sim 8 \text{ V}$, $\frac{df}{dV_g}$ is between $0.2 - 1.5 \text{ MHz/V}$ (see supporting information), which with $|\Delta V| = 1 \text{ V}$ gives a range of $R_f \sim 24 - 181 \text{ MHz/s}$. $\frac{df_0}{dV_g}$ is determined by the device geometry²⁴ and strain, and could be increased by using small area devices or shallower cavities. We note that R_f characterizes the change in the steady-state f_V for a particular dose, not the dynamic change in f_V , which is limited by the RC time constant of the device ($\sim 1 \mu\text{s}$). Still, the frequency tuning rate of phototuning is exceptionally fast; for example, with a moderate bias voltage of $\sim 10 \text{ V}$ and optical power of 1 mW , it is possible to tune a resonator by its full linewidth in $\sim 100 \mu\text{s}$ (10^4 resonators per second) or to enable feedback control with a bandwidth exceeding 10 kHz .

The photodoping rate depends on the device material (graphene vs. gr/hBN), the polarity of ΔV , and the optical power. We measure α with optical power ranging from $20 - 2540 \mu\text{W}$ (see supporting information for full power range) with a blue doping laser (445 nm) and set $V_d = \pm 8 \text{ V}$. The results for two graphene/hBN and three graphene-only devices (Figure 4b-c) show several features. First, the photodoping rate depends on whether $\Delta V < 0$ (α^- branch) or $\Delta V > 0$ (α^+ branch) (Figure 4b). For all devices, $\alpha^+ > \alpha^-$, but the difference can vary greatly. For the gr/hBN devices, $\alpha^+ \sim 2\alpha^-$, while for graphene-only devices $\alpha^+ \sim 10^3 \times \alpha^-$ (Figure 4c). Second, while δV_{mCNP} is less than 15% of V_d for both branches of the gr/hBN devices, this is only true for the slower α^- branch of the graphene devices. For the α^+ branch of the graphene device, δV_{mCNP} can be as large as $\sim 50\%$ of V_d (Figure 4b). Third, both α branches follow a non-linear dependence on the power, $\alpha(P) = \alpha_0 P^\gamma$, where γ is between $1.4 - 1.6$ for gr/hBN devices and $1.2 - 1.7$ for the graphene devices (see supporting information). Figure 4d illustrates an example of $\alpha(P)$ for the α^+ branch of a gr/hBN device with laser power increasing from $20 - 640 \mu\text{W}$, where the black line is a fit with $\gamma = 1.63$. The non-linear dependence on the power shows that the phototuning effect is not purely determined by delivered energy, but is also potentially due to local laser-induced heating of the suspended 2D sheets²⁸, which would lower the energy barrier between the donors (acceptors) and the conduction (valence) bands. Lastly, α for gr/hBN devices is greater than for graphene-only devices, regardless of branch, although the difference is significantly larger for the α^- branch, which can differ by a

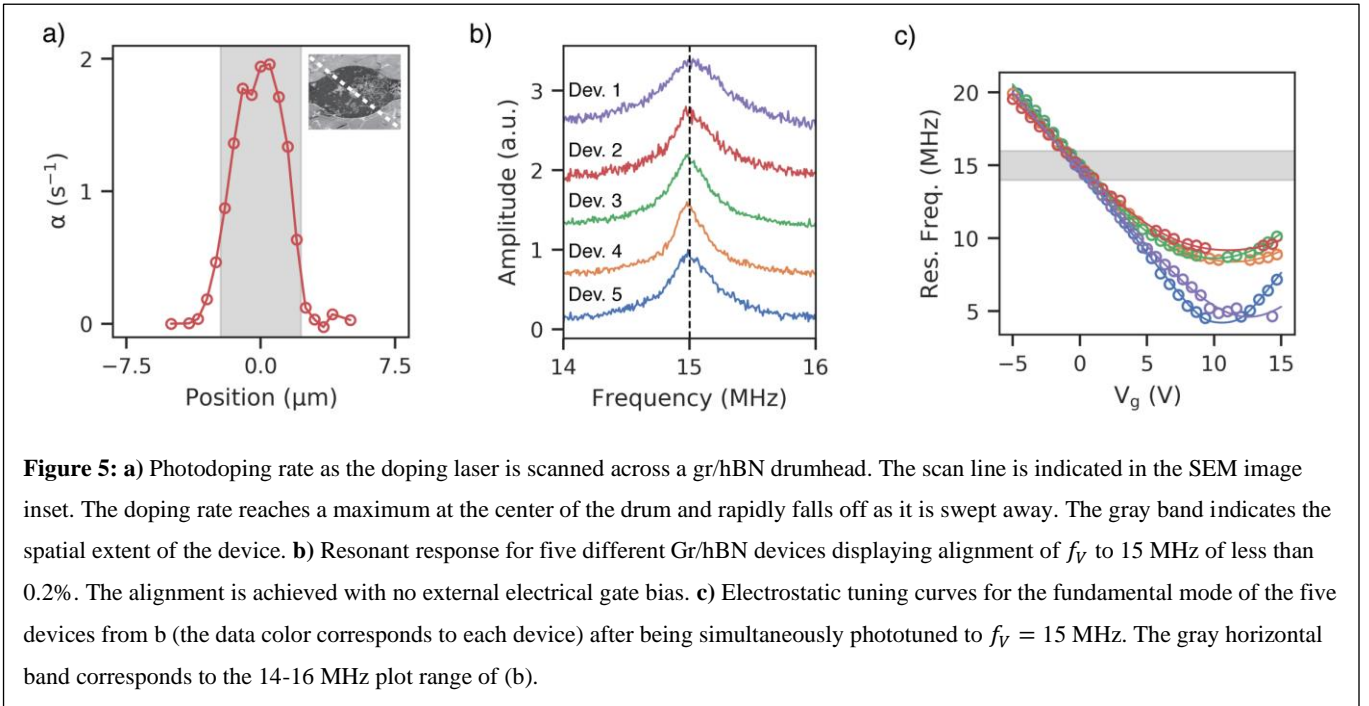
factor of $10^2 - 10^3$ (Figure 4c). The differences in the rates and the value of ΔV between the gr/hBN and graphene-only devices suggests that the gr/hBN heterostructure has a higher density of ionizable dopants and/or a lower dopant ionization energy, consistent with previous reports of electronic photodoping^{32,33}.



The phototuning rate is greater for shorter wavelength light. To characterize the wavelength dependence of α , we measure α in a gr/hBN device using four different laser wavelengths (633, 532, 445, 405 nm) with an optical power of 20 μ W and $|V_d| = 8$ V. The results (Figure 4e) show that shorter wavelength, higher energy illumination leads to much faster phototuning. Compared to 633 nm light ($\alpha^+ = 1.8 \times 10^{-4}$ s⁻¹ and

$\alpha^- = 3.1 \times 10^{-5} \text{ s}^{-1}$), α for 405 nm light ($\alpha^+ = 1.3 \text{ s}^{-1}$ and $\alpha^- = 0.72 \text{ s}^{-1}$) is larger by a factor of $\sim 10^4$.

The rate increase also appears to be saturating near 3 eV. The enhanced phototuning at shorter wavelengths agrees with previous photodoping studies in h-BN as well as SiO_2 ³²⁻³⁴. The wavelength dependence of α is advantageous for nanomechanics experiments, as it allows selection of a long-wavelength laser for transduction, which has a negligible phototuning effect, and a short-wavelength laser for phototuning. We note that higher photon energies likely also induce photodoping, which could explain the frequency shifts seen in γ -ray irradiated 2D sheets⁴⁰.



Many applications in NEMS circuits and lattices require precise, programmable frequency and strain tuning of individual resonators within large arrays on a single chip^{13,37}. To demonstrate this capability with phototuning, we first show that the effect is localized to the laser spot. Figure 5a shows the doping rate at 20 μW measured at different locations on the membrane. The device begins to photodope only when the gaussian spot of the laser overlaps with the area of the membrane. We use the dilation of the spatial doping rate profile relative to the device diameter (greyed region in Figure 5a) to infer a spatial resolution of $\sim 1 \mu\text{m}$, which is approximately the size of the laser spot. Next, we align the frequencies of five different gr/hBN devices, which are all on a single chip, to within 30 kHz (or 0.2%) of $f_V = 15 \text{ MHz}$, as shown in

the Figure 5b amplitude spectra, achieving a tuning precision within $\sim 5\%$ of a resonance linewidth. The resonance frequency gate curves for each device are shown in Figure 5c. While the curves intersect at $V_g = 0$ V, which defines f_V , the values of V_{mCNP} and the general curve shape vary considerably. This demonstrates that phototuning is largely insensitive to variations between individual resonators and is thus a robust frequency tuning method.

The phototuning effect we demonstrate in graphene and gr/hBN NEMS could be applicable to other NEMS as well. Persistent photodoping has been observed in a variety of graphene heterostructures^{33,34,41} as well as other materials including SrTiO₃⁴². In these systems, the mechanical element does not need to be graphene or an atomically thin graphene hybrid. For example, graphene-coated silicon nitride nanobeams⁴³ could be persistently tuned but would retain ultra-high quality factors of $Q > 10^6$. However, atomically thin resonators have the great advantage of an extreme tuning range.

Phototuning offers intriguing possibilities for both applied and fundamental physics in isolated NEMS and NEMS arrays, where tight control over individual resonators is essential. Our technique can pattern arbitrary complex geometries of static charge across a single, large-area resonator, which could improve the actuation efficiency of antisymmetric modes or allow tunable intermodal coupling³¹, both commonly achieved via intricately patterned back-gates. Furthermore, this tuning also offers new opportunities for programmable NEMS crystals. In our vision for these crystals, individual resonators would be coupled to neighboring resonators by a suspended bridge material. By phototuning the resonators and the bridges, precisely tuned complex acoustic crystals would be possible. Unlike previous demonstrations of static phononic crystals⁵ and tunable phononic crystals¹⁶, our approach is not vulnerable to fabrication imperfections and possesses a higher degree of tunability and the ability to modify individual unit cells of the crystal.

Finally, due to the high spatial resolution and large tuning rates, phototuning also permits high-density analog mechanical memory storage, where information is encoded in the frequency of each resonator. If

each memory state is separated by a resonance linewidth (~ 100 kHz), the tuning range demonstrated in Figure 3a would accommodate ~ 500 states, equivalent to a 9-bit memory. Given the measured tuning rates of 1 GHz/s, the state of a single device could be uniformly tuned by a linewidth ($f_V/Q \sim 100$ kHz) in ~ 100 μ s. Even faster tuning control should be possible with higher laser power since both graphene and h-BN are stable at high temperatures⁴⁴.

In conclusion, we have demonstrated a fast, reversible, persistent, and scalable frequency tuning method based on deterministic charge trapping, which allows for electro-optic “etch-a-sketch” patterning of strain in 2D NEMS arrays. Our phototuning technique eliminates the need for complex, lithographically defined gate electrodes used to electrostatically strain and frequency tune NEMS resonators. When applied to large NEMS lattices, this approach could enable reprogrammable phononic crystals and waveguides^{16,37}, or more exotic applications such as nanomechanical logic, neuromorphic computing^{17,18}, or the simulation of complex networks¹⁹.

METHODS:

Fabrication of 2D drumheads:

gr/h-BN mechanical drumhead resonators were fabricated by transferring the 2D sheets over an array of cavities etched into 1 μ m wet thermal oxide^{45,46} grown on degenerately doped silicon wafers (University Wafer). The cavities were fabricated using direct-write optical lithography and CHF_3 based reactive ion etching. A ~ 300 nm layer of oxide was left at the bottom of the cavity to act as a charge trapping layer and to prevent shorting. Ti/Pt electrodes were defined by lithography and deposited by electron-beam evaporation.

To prepare the 2D sheets for transfer, a relatively thick layer (~ 3 μ m) of PMMA A11 was spun onto CVD grown single-layer h-BN on Cu foil (Graphene Supermarket) and then a polyamide scaffold with a central hole removed was then placed on the PMMA/hBN/Cu stack. The stack was placed in a bath of Ammonium Persulphate to etch the Cu and then rinsed in deionized water and dried in air. The polyamide/PMMA/hBN

was placed on top of CVD graphene grown on Cu foil (Graphenea) and baked at 180 °C for 30 minutes to adhere the hBN and the graphene⁴⁶. The etching, rinsing, and drying was repeated leaving a freestanding film of PMMA/hBN/Graphene supported by the polyamide scaffold. To transfer the 2D sheets to the cavity substrates, the PMMA/hBN/Graphene stack was then placed graphene-side-down on top of the pre-patterned cavities and adhered at 155 °C overnight (~15 hours). After removing the polyamide scaffold, the PMMA was removed in flowing Ar/H₂ at 400 °C. The graphene sheet contacts the electrodes from above, resulting in a simultaneous electrical connection to all devices. Graphene-only devices were fabricated in a similar fashion with both an in-house and a commercial transfer process performed by Graphenea.

Measurement of mechanical motion:

Device motion was measured using optical interferometry, as described previously²⁸. A 633 nm HeNe laser was focused onto the devices (held at room temperature at 10⁻⁶ torr) using a 40 ×, 0.6 NA objective. The reflected light was detected using a high-sensitivity photodiode (Thorlabs APD 130A) and the voltage signal was demodulated using a Zurich Instruments HFLI2 Lock-In amplifier. The incident laser was scanned with a two-axis galvometer and passed through an optical relay system in order to image the mode shape and to maximize transduction sensitivity. We used low laser power (~1 – 10 μW) to avoid unwanted photodoping by the 633 nm probe laser.

Photodoping:

A separate laser (405 nm, 445 nm, or 532 nm) was used for photodoping. The doping laser was coupled into the beam-path using a dichroic mirror and focused onto the sample using the same 40 ×, 0.6 NA objective lens. A separate two-axis galvometer was used to position the doping laser at the center of the drumheads. The laser power for each color was calibrated using a power meter (Thorlabs 120VC) and maintained using PID control. For dynamic measurements of V_{mCNP} , an acousto-optic modulator (AA-Optoelectronics MT350-A0.12-VIS) was used to supply a well-defined pulse of the doping laser with pulse-widths down to ~10 ns. Prior to all measurements, the doping laser was scanned across the device with $V_d = 0$ V to guarantee a uniformly doped initial erased state.

SUPPORTING INFORMATION:

Method for measuring V_{mCNP} , diagram of optical setup, long-term stability of phototuning, measurement of $\frac{df_0}{dV_g}$, and doping rate as function of laser power.

AUTHOR INFORMATION:

Corresponding Author:

Benjamín Alemán

*baleman@uoregon.edu

AUTHOR CONTRIBUTIONS:

DM and BA conceived and designed the experiments. DM and AB fabricated the NEMS devices. DM designed and built optical measurement apparatus and performed the experiments with assistance from AB. DM analyzed the data. DM and BA wrote the manuscript, and AB provided comments on the manuscript. BA supervised the work.

ACKNOWLEDGMENTS:

We acknowledge the facilities and staff from the Center for Advanced Materials in Oregon (CAMCOR), and the use of the University of Oregon's Rapid Materials Prototyping facility, funded by the Murdock Charitable Trust. We thank Joshua Ziegler, Rudy Resch, and Kara Zappitelli for scientific discussions and feedback related to this work. This work was supported by the University of Oregon and the National Science Foundation (NSF) under grant No. DMR-1532225.

REFERENCES:

- (1) Jensen, K.; Kim, K.; Zettl, A. *Nat. Nanotechnol.* **2008**, 3 (9), 533–537.
- (2) Steele, G. A.; Huttel, A. K.; Witkamp, B.; Poot, M.; Meerwaldt, H. B.; Kouwenhoven, L. P.; van

- der Zant, H. S. J. *Science* **2009**, 325 (5944), 1103–1107.
- (3) Degen, C. L.; Poggio, M.; Mamin, H. J.; Rettner, C. T.; Rugar, D. *Proc Natl Acad Sci U S A* **2009**, 106 (5), 1313–1317.
 - (4) Okamoto, H.; Gourgout, A.; Chang, C.-Y.; Onomitsu, K.; Mahboob, I.; Chang, E. Y.; Yamaguchi, H. *Nat. Phys.* **2013**, 9 (8), 480–484.
 - (5) Chan, J.; Alegre, T. P. M.; Safavi-Naeini, A. H.; Hill, J. T.; Krause, A.; Gröblacher, S.; Aspelmeyer, M.; Painter, O. *Nature* **2011**, 478 (7367), 89–92.
 - (6) Dominguez-Medina, S.; Fostner, S.; Defoort, M.; Sansa, M.; Stark, A.; Halim, M. A.; Vernhes, E.; Gely, M.; Masselon, C.; Hentz, S. *Science* **2018**, 362 (November), 918–922.
 - (7) Ekinci, K. L.; Roukes, M. L. *Rev. Sci. Instrum.* **2005**, 76 (6), 061101.
 - (8) Yao, A.; Hikiyara, T. *Appl. Phys. Lett.* **2014**, 105 (12), 123104.
 - (9) Rueckes, T., Kyoungha Kim, Ernesto Joselevich, Greg Y. Tseng, Chin-Li Cheung, C. M. L. *Science* **2000**, 289 (5476), 94–97.
 - (10) Masmanidis, S.; Masmanidis, S.; Karabalin, R.; Vlaminck, I.; Borghs, G.; Freeman, M.; Roukes, M. *Science* **2007**, 317 (5839), 780–783.
 - (11) Hafiz, M. A. A.; Kosuru, L.; Younis, M. I. *J. Appl. Phys.* **2016**, 120 (7).
 - (12) Roukes, M. L. *IEDM Tech. Dig.* **2004**, No. December 13-15, 539–542.
 - (13) Cha, J.; Daraio, C. *Nat. Nanotechnol.* **2018**, 13 (11), 1016–1020.
 - (14) Olsson, R. H.; El-Kady, I. *Meas. Sci. Technol.* **2009**, 20 (1).
 - (15) Wang, Y.; Yousefzadeh, B.; Chen, H.; Nassar, H.; Huang, G.; Daraio, C. *Phys. Rev. Lett.* **2018**, 121 (19), 194301.
 - (16) Cha, J.; Kim, K. W.; Daraio, C. *Nature* **2018**, 564 (7735), 229–233.

- (17) Hoppensteadt, F. C.; Izhikevich, E. M. *IEEE Trans. Circuits Syst. I Fundam. Theory Appl.* **2001**, *48* (2), 133–138.
- (18) Kumar, A.; Mohanty, P. *Sci. Rep.* **2017**, *7* (1), 1–9.
- (19) Matheny, M. H.; Emenheiser, J.; Fon, W.; Chapman, A.; Salova, A.; Rohden, M.; Li, J.; Hudoba de Badyn, M.; Pósfai, M.; Duenas-Osorio, L.; Mesbahi, M.; Crutchfield, J. P.; Cross, M. C.; D’Souza, R. M.; Roukes, M. L. *Science* **2019**, *363* (6431), eaav7932.
- (20) Zhang, W.-M.; Hu, K.-M.; Peng, Z.-K.; Meng, G. *Sensors (Basel)*. **2015**, *15* (10), 26478–26566.
- (21) Bunch, J. S.; Van Der Zande, A. M.; Verbridge, S. S.; Frank, I. W.; Tanenbaum, D. M.; Parpia, J. M.; Craighead, H. G.; McEuen, P. L. *Science* **2007**, *315* (January), 490–493.
- (22) Merced, E.; Cabrera, R.; Dávila, N.; Fernández, F. E.; Sepúlveda, N. *Smart Mater. Struct.* **2012**, *21* (3).
- (23) Chiao, M.; Lin, L. *J. Micromechanics Microengineering* **2004**, *14* (12), 1742–1747.
- (24) Chen, C.; Rosenblatt, S.; Bolotin, K. I.; Kalb, W.; Kim, P.; Kymissis, I.; Stormer, H. L.; Heinz, T. F.; Hone, J. *Nat. Nanotechnol.* **2009**, *4* (12), 861–867.
- (25) Enderling, S.; Hedley, J.; Jiang, L.; Cheung, R.; Zorman, C.; Mehregany, M.; Walton, A. J. *J. Micromechanics Microengineering* **2007**, *17* (2), 213–219.
- (26) Kim, K.; Jensen, K.; Zettl, A. *Nano Lett.* **2009**, *9* (9), 3209–3213.
- (27) Chang, J.; Koh, K.; Min, B. K.; Lee, S. J.; Kim, J.; Lin, L. *ACS Appl. Mater. Interfaces* **2013**, *5* (19), 9684–9690.
- (28) Davidovikj, D.; Slim, J. J.; Cartamil-Bueno, S. J.; van der Zant, H. S. J.; Steeneken, P. G.; Venstra, W. J. *Nano Lett.* **2016**, *16* (4), 2768–2773.
- (29) Song, X.; Oksanen, M.; Sillanpää, M. A.; Craighead, H. G.; Parpia, J. M.; Hakonen, P. J. *Nano Lett.* **2012**, *12* (1), 198–202.

- (30) Will, M.; Hamer, M.; Müller, M.; Noury, A.; Weber, P.; Bachtold, A.; Gorbachev, R. V.; Stampfer, C.; Güttinger, J. *Nano Lett.* **2017**, *17* (10), 5950–5955.
- (31) De Alba, R.; Massel, F.; Storch, I. R.; Abhilash, T. S.; Hui, A.; McEuen, P. L.; Craighead, H. G.; Parpia, J. M. *Nat. Nanotechnol.* **2016**, *11* (9), 741–746.
- (32) Ju, L.; Velasco, J.; Huang, E.; Kahn, S.; Nosiglia, C.; Tsai, H.-Z.; Yang, W.; Taniguchi, T.; Watanabe, K.; Zhang, Y.; Zhang, G.; Crommie, M.; Zettl, A.; Wang, F. *Nat. Nanotechnol.* **2014**, *9* (May).
- (33) Kim, Y. D.; Bae, M.-H.; Seo, J.-T.; Kim, Y. S.; Kim, H.; Lee, J. H.; Ahn, J. R.; Lee, S. W.; Chun, S.-H.; Park, Y. D. *ACS Nano* **2013**, *7* (7), 5850–5857.
- (34) Choi, H. H.; Park, J.; Huh, S.; Lee, S. K.; Moon, B.; Han, S. W.; Hwang, C.; Cho, K. *ACS Photonics* **2018**, *5* (2), 329–336.
- (35) Neumann, C.; Rizzi, L.; Reichardt, S.; Terrés, B.; Khodkov, T.; Watanabe, K.; Taniguchi, T.; Beschoten, B.; Stampfer, C. *ACS Appl. Mater. Interfaces* **2016**, *8* (14), 9377–9383.
- (36) Velasco, J.; Ju, L.; Wong, D.; Kahn, S.; Lee, J.; Tsai, H. Z.; Germany, C.; Wickenburg, S.; Lu, J.; Taniguchi, T.; Watanabe, K.; Zettl, A.; Wang, F.; Crommie, M. F. *Nano Lett.* **2016**, *16* (3), 1620–1625.
- (37) Hatanaka, D.; Bachtold, A.; Yamaguchi, H. *Phys. Rev. Appl.* **2019**, *11* (2), 024024.
- (38) Schedin, F.; Geim, A. K.; Morozov, S. V.; Hill, E. W.; Blake, P.; Katsnelson, M. I.; Novoselov, K. S. *Nat. Mater.* **2007**, *6* (9), 652–655.
- (39) Mahboob, I.; Yamaguchi, H. *Nat. Nanotechnol.* **2008**, *3* (5), 275–279.
- (40) Lee, J.; Krupcale, M. J.; Feng, P. X. L. *Appl. Phys. Lett.* **2016**, *108* (2).
- (41) Ho, P.-H.; Chen, C.-H.; Shih, F.-Y.; Chang, Y.-R.; Li, S.-S.; Wang, W.-H.; Shih, M.-C.; Chen, W.-T.; Chiu, Y.-P.; Li, M.-K.; Shih, Y.-S.; Chen, C.-W. *Adv. Mater.* **2015**, *27* (47), 7809–7815.

- (42) Yeats, A. L.; Pan, Y.; Richardella, A.; Mintun, P. J.; Samarth, N.; Awschalom, D. D. *Sci. Adv.* **2015**, *1* (9), e1500640.
- (43) Verbridge, S. S.; Parpia, J. M.; Reichenbach, R. B.; Bellan, L. M.; Craighead, H. G. *J. Appl. Phys.* **2006**, *99* (12).
- (44) Ye, F.; Lee, J.; Feng, P. X.-L. *Nano Lett.* **2018**, *18* (3), 1678–1685.
- (45) Suk, J. W.; Kitt, A.; Magnuson, C. W.; Hao, Y.; Ahmed, S.; An, J.; Swan, A. K.; Goldberg, B. B.; Ruoff, R. S. *ACS Nano* **2011**, *5* (9), 6916–6924.
- (46) Shautsova, V.; Gilbertson, A. M.; Black, N. C. G.; Maier, S. A.; Cohen, L. F. *Sci. Rep.* **2016**, *6* (1), 30210.

TABLE OF CONTENTS GRAPHIC:

